International Journal of Heat and Mass Transfer 145 (2019) 118672

Contents lists available at ScienceDirect

International Journal of Heat and Mass Transfer

journal homepage: www.elsevier.com/locate/ijhmt

Modeling of water evaporation from a shrinking moist biomass slab subject to heating: Arrhenius approach versus equilibrium approach ☆

Peyman Rahimi Borujerdi [a], Babak Shotorban [a,*], Shankar Mahalingam [a], David R. Weise [b]

[a] Department of Mechanical and Aerospace Engineering, The University of Alabama in Huntsville, Huntsville, AL 35899, USA
[b] Pacific Southwest Research Station, USDA Forest Service, Riverside, CA 92507, USA

ARTICLE INFO

Article history:
Received 22 April 2019
Received in revised form 24 August 2019
Accepted 31 August 2019
Available online 20 September 2019

Keywords:
Gpyro
Liquid moisture
Evaporation
Fuel moisture content
Equilibrium model
Arrhenius model
Shrinkage

ABSTRACT

Liquid moisture evaporation and pyrolysis of a biomass fuel slab subject to heating were computationally investigated in a one-dimensional domain where the fuel shrinkage was accounted for. The evaporation dynamics was separately represented by equilibrium and Arrhenius models. The equilibrium model describes evaporation as a thermodynamic process whereas the Arrhenius model treats it as a chemical reaction. For calculations, Gpyro, a pyrolysis computational framework, was used after its source code was revised to include the equilibrium model. By default, Gpyro is only capable of operating with the Arrhenius model. In the present study, also, a continuum description of mass and energy conservation for a pyrolyzating, shrinking porous medium was provided in the form of integral-differential equations. Such a description in the previous Gpyro works was lacking for shrinking objects and the Gpyro documents only provided a numerically discretized equation form. Here, the approximations made to develop this form from the integral-differential equations were clarified. The model was validated against experimental data of cone calorimeter experiments. Two fuel moisture contents (FMC) of 26% and 100% (on dry basis) representing dead and living fuels, respectively, were examined. The living fuel is characterized by a high FMC although the difference between dead and living fuels is not limited to this parameter. The evaporation rate, liquid moisture mass fraction and temperature profiles obtained by using the equilibrium model exhibited abrupt changes at the evaporation front whereas those obtained by using the Arrhenius model showed a smooth behavior throughout the slab. The drying dynamics described by the equilibrium model was more consistent with the underlying physics of evaporation. The equilibrium model demonstrated a distinct evaporation front, did not result in evaporation below the normal boiling point of water and more accurately exhibited the impact of the initial FMC on the drying dynamics. Simulation results showed that the thermochemical evolution of living fuel was appreciably more sensitive to the evaporation model.

1. Introduction

Wildland fire is prevalent in many areas of the world affecting ecosystems in different ways [1]. This natural phenomenon may have major detrimental impacts on wildlife, human life, air quality and economy. On the other hand, wildland fire may have beneficial effects such as reducing fire risk by removing accumulated organic material, improving site productivity by releasing nutrients, improving plant community health by eliminating diseases, and creating favorable habitat conditions for various flora and fauna. The fuel source for wildland fire is vegetative biomass possessing a wide variety of properties which influence water content and processes such as absorption, transpiration and evaporation [2], pyrolysis, ignition time, flame formation, and fire spread [3]. Several studies have shown that the main constituents of biomass fuels are cellulose, hemicellulose and lignin [4] (and references therein). Living biomass also contains sugars, lipids, proteins, macro and micronutrients [5]. Liquid water is another constituent of wildland fuels. The liquid water amount in a wildland fuel can be quantified by the fuel moisture content (FMC) defined here as the ratio of the mass of liquid water contained in the fuel to the mass of dry fuel. In the case of living fuels, FMC ranges from around 50% up to 300% for some succulent plants while dead fuel FMC rarely exceeds 30% [6]. Liquid moisture has a relatively large latent heat of vaporization. As a result, the thermal load for complete evaporation is around 30% of the sensible heat required by the

☆ This manuscript prepared, in part, by a U.S. Government employee on official time, is not subject to copyright and is in the public domain.

* Corresponding author.
E-mail address: babak.shotorban@uah.edu (B. Shotorban).

https://doi.org/10.1016/j.ijheatmasstransfer.2019.118672
0017-9310/

Nomenclature

D	diffusion coefficient
E	activation energy
h_c	convective heat transfer coefficient
h_i	sensible enthalpy of the condensed phase species i
h_m	mass transfer coefficient
Δh_e	heat of evaporation
Δh	heat of reaction
$\dot{j}''$	diffusive mass flux
K	number of heterogeneous reactions
M	number of condensed phase species
$\bar{M}$	mean molecular weight
M_v	water vapor molecular weight
$\dot{m}''$	convective mass flux
N	number of gas phase species
P	pressure
$\dot{Q}_{s\text{-}g}$	volumetric rate of heat transfer from the condensed phase to the gas phase
$\dot{Q}'''_{s,k}$	heat release from or absorption to the condensed phase due to the heterogeneous reaction k
$\dot{q}''$	conduction heat flux
$\dot{q}''_e$	incident radiant heat flux
$\dot{q}''_r$	in-depth radiation heat flux
$\dot{q}''_t$	total heat flux
R	universal gas constant
T	temperature
t	time variable
Δt	time step
U	fuel moisture content
V_c	condensed phase absolute velocity
V	gas phase absolute velocity
v_j	absolute velocity of the gaseous species j
Y	mass fraction
z	coordinate
Δz	size of a computational cell
Z	pre-exponential factor

Greek symbols

α	surface absorptivity
ϵ	surface emissivity
ρ_g	gas phase density
ρ_v	water vapor density
σ	Stefan-Boltzman constant
τ	slab thickness
$\bar{\psi}$	mean porosity
$\dot{\omega}'''_{fi}$	rate of formation of the condensed phase species i
$\dot{\omega}'''_{di}$	rate of destruction of the condensed phase species i
$\dot{\omega}'''_{fj}$	rate of formation of the gas phase species j
$\dot{\omega}'''_{dj}$	rate of destruction of the gas phase species j

Subscript

B	center of the bottom computational cell
b	bottom
i	condensed phase species index
j	gas phase species index
P	computational cell center
T	center of the top computational cell
t	top

Superscripts

0	value of the variable in the previous time step
$*$	value of the variable in the reaction stage

moist particle to reach the pyrolysis temperature [7]. Therefore, drying is a critical stage in the process of thermal decomposition and devolatilization of living fuels and can have a significant impact on the ignition and subsequent combustion of pyrolysis gases. This, indeed, highlights a need for studying the role of FMC and evaporation in wildland fuels in more details.

The influence of FMC on the thermochemical evolution of biomass has been studied extensively. Bryden and Hagge [8] computationally studied the combined effects of fuel moisture content and fuel shrinkage on the pyrolysis of a biomass particle. Liquid moisture was converted to water vapor through a chemical reaction like term and shrinkage factor was defined as the final thickness to the initial thickness of the particle. They concluded that the influence of moisture content and shrinkage depended on the pyrolysis regime which is identified by the Biot number. For instance, the impact of shrinkage on the pyrolysis time was negligible and independent of the moisture content in the thermally thin regime whereas both shrinkage and moisture content substantially affected the pyrolysis time in the thermally thick regime. Moreover, it was shown that when fuel shrinkage and moisture content were coupled, tar yield increased while light hydrocarbon yield decreased. Ferguson et al. [9] investigated the effect of gaseous water released from liquid moisture evaporation on combustion of gas mixtures through modeling of premixed and diffusion flames. The flame peak temperature increased as the amount of water vapor in the fuel stream decreased and an upper limit existed for the water vapor mole fraction above which combustion did not occur. Moreover, premixed flame simulations showed that the flame speed and the peak heat release rate were reduced by increasing the water vapor mole fraction in the fuel mixture. Bates and Ghoniem [7] studied the impacts of external source temperature, particle size and FMC on biomass torrefaction. They introduced a drying sub-model based on the Arrhenius kinetic rate which neglected structural changes. The results indicated that the biomass heat up time increased linearly with FMC and quadratically with the particle size and it exhibited more sensitivity to the change in FMC for larger particles. The mass loss evolution of the small particle was insensitive to FMC. Shotorban et al. [10] investigated the effects of FMC on pyrolysis and ignition of a cellulosic leaf-like fuel element subjected to convective heating. They modeled evaporation as a kinetic process added to the overall reaction scheme. Volume change of the element was ignored. Results showed that as the FMC decreased, the temperature and the decomposition rate increased. Around the ignition point, water was fully vaporized while it remained elsewhere. Substantial volume fraction of water vapor both nearby and away from the combustion zone indicated that evaporation and ignition could occur simultaneously.

Researchers have used three approaches to model liquid moisture evaporation in vegetative and biomass fuels. The most common approach is the Arrhenius model [11,8,12,13,14]. In this model, the evaporation rate is governed by a first order kinetic equation based on the well-known Arrhenius law, which makes it a computationally straightforward approach. Indeed, the basis of the Arrhenius model is a physical chemistry principle which states that removal of liquid water from a moist particle can be explained by applying the activation energy concept [15]. Then reaction engineering can be used to determine the rate of water

removal. As it will be shown in Section (4), liquid moisture evolution determined by the Arrhenius model exhibits smooth gradients, which facilitates numerical stability. This favorable feature, however, is achieved at the expense of some drawbacks. Most importantly, this model treats evaporation as a kinetic process whereas in reality it is a thermodynamic process. Moreover, a unique set of the kinetic parameters, i.e. the pre-exponential factor and the activation energy, appropriate for liquid moisture evaporation, cannot be found in the literature [11,16,17]. Also, the large gradients of the liquid moisture and the steepness of the evaporation front which are characteristics of high temperature and/or high heating rate drying scenarios [18] are not captured by the Arrhenius model. Lastly, it does not predict the low temperature behavior accurately since it results in evaporation of considerable amount of the liquid moisture at temperatures below the water normal boiling point [19]. Similar to the Arrhenius approach, the reaction engineering approach (REA) [15,20,21] treats evaporation and condensation as competitive reactions. In this approach, the evaporation process is assumed as a zero-order kinetics and the condensation process is assumed as a first-order kinetics with their corresponding activation energies. The L-REA and S-REA are suitable for thermally thin and thick samples, respectively.

Another approach is the heat sink model [22–26], which assumes that evaporation takes place at a fixed boiling temperature. When the temperature reaches the boiling point, all supplied heat is used to completely vaporize water. Indeed, evaporation behaves like a heat sink. In the heat sink model, evaporation is completely controlled by heat transfer [27] by assuming that there is no resistance to water vapor mass transfer and it immediately leaves the particle as it is formed. One way to implement this model is to assume the evaporation front to be infinitesimally thin and divide the particle into a wet and a completely dried zones [28,29]. To incorporate this approach in computations, one needs to track a moving boundary that separates the dry and wet zones which is not trivial to deal with. On the other hand, the assumption of infinitely thin evaporation front is not necessarily valid as the front can have a finite thickness comparable to the particle size [16]. Another way to implement the heat sink model is to use a conditional energy equation [27], in which when the temperature reaches water boiling point, the time derivative of temperature is set to zero and the evaporation rate is calculated. The condition can also be placed on the equation that calculates the evaporation rate [24,26]. This approach is not computationally efficient since the condition introduces a sharp discontinuity to the equations [19,27].

The third approach called the equilibrium model [30–36] is based on the fact that evaporation is a phase change process and probably, the most significant physical aspect of such process which is neglected by the previously discussed models, is the saturation condition at which both phases (here liquid moisture and water vapor) exist at thermodynamic equilibrium. Since this approach is physically more robust it does not exhibit the downsides of the Arrhenius and the heat sink models. However, the implementation of the equilibrium model in the computations is significantly more involved.

The Arrhenius and the equilibrium models use two different methods to calculate the evaporation rate and the water vapor density. Treating the evaporation akin to a chemical reaction, in the Arrhenius model the evaporation rate is calculated by the well known Arrhenius kinetic equation and expressed in terms of apparent density of liquid moisture and temperature. Subsequently, the water vapor density is obtained from the corresponding mass conservation equation. On the other hand, in the equilibrium model, the water vapor density is no longer an independent variable and indeed constrained by a thermodynamic equilibrium equation which correlates the vapor partial pressure to the local temperature and moisture content [37,38]. Then, the evaporation rate is obtained using the water vapor mass conservation equation. The constraint, which is in the form of an algebraic equation, is coupled to the conservation law equations, which are in the form of differential equations. Hence, a system of Differential-Algebraic Equations (DAE) [33,27] represents the whole thermochemical process. Some researchers [39,33] solved this DAE system, using the DASSL program [40]. Di Blasi [31], however, utilized the method of operator splitting to solve it. The basis for this method is to "split" the time evolution of the process into partial steps, each accounting for a specific sub-process [41]. For example, the operator splitting technique is common in numerical solution of coupled reaction-diffusion-advection problems such as reactive flow and air pollution problems [42,43]. Alternative to the method described above on computing evaporation rate when equilibrium condition prevails, one may assume that the evaporation rate is proportional to the difference between the equilibrium and the instantaneous water vapor densities and then find the rate by using an appropriate proportionality constant [34,35,38]. Although Wurzenberger et al. [34] and Zobel [35] still classify this method as an equilibrium approach, Massman [38] who introduces a dynamic condensation coefficient into the rate equation, refers to this method as a non-equilibrium approach.

In this work, both the drying and pyrolysis of a moist shrinking biomass slab exposed to radiant heating were numerically investigated. The liquid moisture evaporation from the slab was studied using both the Arrhenius and the equilibrium models. A detailed comparison was performed between the two aforesaid methods at two different FMC's corresponding to dead and living fuels to examine the effects of the evaporation modeling approach and FMC on the drying dynamics and thermal decomposition of a biomass particle. Here, Gpyro [44], an open source computer model, was used for computations. Gpyro describes the thermal responses of materials to heating while accounting for heat and mass transfer within the material and pyrolysis of the condensed phase. The heterogeneous chemical reactions, which involve the destruction of a condensed phase species to form gases and/or additional condensed phase species, can be set up in Gpyro using input chemical kinetic parameters. To represent moisture evaporation using the Arrhenius method in Gpyro, it was treated as a heterogeneous reaction in the current study (see Section 2.2.1) with kinetic parameters given in Section 3. The Arrhenius approach was also used for moisture evaporation with Gpyro in the previous studies of smoldering combustion [45–47] and bench-scale pyrolysis of lignocellulosic biomass [48]. To equip Gpyro with the equilibrium model (see Section 2.2.2) for moisture evaporation, substantial changes were made in the source code in the current study, as illustrated in Section 2.4. Also, a continuum description of mass and energy conservation for a pyrolyzating, shrinking porous medium was provided in the form of integral-differential equations (see §§2.1). Such a description in the previous Gpyro works was lacking for shrinking medium, and under the shrikage assumption, the Gpyro developers [13,44] only provided a numerically discretized equation form. Here, the approximations made to derive this form from the integral-differential equations were clarified in Section 2.3. It is noted that there are also differential equations given under no volume change (no shrinkage or swelling) assumption by the Gpyro developers [49,44]. However, Refs. [45–47] presented these differential equations as the governing equations while assuming and discussing the shrinkage. Presumably, this contradiction was the consequence of an oversight in identifying and/or presenting what equations the Gpyro software solved under the shrinkage assumption. Hence, the data generated by Gpyro in these references may not have been in conflict with this assumption.

2. Mathematical and computational approaches

2.1. Mass and energy conservation equations

The mass and energy conservation laws for a pyrolyzing, shrinking (or swelling) porous medium are shown in this section. Here, the (macroscopic) spatial variation of the medium is assumed to only occur in one dimension, corresponding to the z coordinate. The transport of the liquid phase is assumed negligible. Both solid and liquid phases are referred to as the condensed phase. The assumption of negligible liquid transport is reasonable when the pressure inside the porous medium does not considerably exceed the ambient pressure. However, when high internal pressure is developed inside the medium, the transport of the liquid phase becomes significant [50].

Let $z_t(t)$ and $z_b(t)$ represent the material coordinates (Lagrangian coordinates) of two arbitrary points (top and bottom points) on the condensed phase at time t. Conservation of the condensed phase mass for a domain limited between these two points, as a control mass (system), is expressed by

$$\frac{d}{dt}\int_{z_t(t)}^{z_b(t)} \bar{\rho} dz = -\int_{z_t(t)}^{z_b(t)} \dot{\omega}_{fg}''' dz, \tag{1}$$

where d/dt is the material time derivative (Lagrangian derivative), $\bar{\rho}$ is the weighted bulk (overall apparent) density of the condensed phase and $\dot{\omega}_{fg}''' = \sum_{k=1}^{K} \dot{\omega}_{fg,k}'''$ is the net mass reduction rate (destruction minus formation) of the condensed phase per unit volume. The notation used for variables in this subsection is consistent with that in [44]. In Eq. (1), $\dot{\omega}_{fg,k}'''$ is the volatilization rate in the heterogeneous reaction k. It is noted that the direction of positive z axis is from top to bottom. The equation for conservation of mass of the condensed phase species i follows a similar form

$$\frac{d}{dt}\int_{z_t(t)}^{z_b(t)} Y_i \bar{\rho} dz = \int_{z_t(t)}^{z_b(t)} \dot{\omega}_i''' dz, \tag{2}$$

where $Y_i\bar{\rho}$ is the density of the species i (mass of particles of the species i per unit volume) and $\dot{\omega}_i''' = \dot{\omega}_{fi}''' - \dot{\omega}_{di}'''$ is the net mass formation rate of the species i per unit volume. The conservation of energy for the condensed phase reads

$$\frac{d}{dt}\int_{z_t(t)}^{z_b(t)} \bar{h}\bar{\rho} dz = -\dot{q}_t''\big|_{z_b(t)} + \dot{q}_t''\big|_{z_t(t)} - \int_{z_t(t)}^{z_b(t)} \dot{Q}_{s\text{-}g}''' dz + \sum_{k=1}^{K}\int_{z_t(t)}^{z_b(t)} \dot{Q}_{s,k}''' dz + \sum_{i=1}^{M}\int_{z_t(t)}^{z_b(t)} \dot{\omega}_i''' h_i dz, \tag{3}$$

where $\bar{h} = \sum_{i=1}^{M} Y_i h_i$ is the total sensible enthalpy, $\dot{q}_t''$ is the combination of conduction and in-depth radiation fluxes. Here, $\dot{Q}_{s-g}'''$ is the volumetric rate of heat transfer from the condensed phase to the gas phase and $\dot{Q}_{s,k}'''$ is the heat release from or absorption to the condensed phase due to the heterogeneous reaction k. In Eq. (3), the contributions of kinetic and potential energies, and work done are ignored.

For the gas phase, the conservation of mass equation is expressed for a control volume limited between $z_t(t)$ and $z_b(t)$

$$\frac{d}{dt}\int_{z_t(t)}^{z_b(t)} \rho_g \bar{\psi} dz + \rho_g \bar{\psi} V_r\Big|_{z_b(t)} - \rho_g \bar{\psi} V_r\Big|_{z_t(t)} = \int_{z_t(t)}^{z_b(t)} \dot{\omega}_{fg}''' dz, \tag{4}$$

where $V_r = V - V_c$ is the gas phase velocity relative to the condensed phase velocity, $\bar{\psi}$ is the mean porosity of species, and ρ_g is the gas phase density. Similarly, for the conservation of mass of the gaseous species j, one will have

$$\frac{d}{dt}\int_{z_t(t)}^{z_b(t)} Y_j \rho_g \bar{\psi} dz + \rho_g Y_j \bar{\psi} v_{jr}\Big|_{z_b(t)} - \rho_g Y_j \bar{\psi} v_{jr}\Big|_{z_t(t)} = \int_{z_t(t)}^{z_b(t)} \dot{\omega}_j''' dz, \tag{5}$$

where Y_j is the mass fraction of the gaseous species j, $v_{jr} = v_j - V_c$ is the velocity of the gaseous species j relative to the condensed phase velocity and $\dot{\omega}_j''' = \dot{\omega}_{fj}''' - \dot{\omega}_{dj}'''$ is the net mass formation rate of the species j per unit volume. The gas phase is assumed to be in thermal equilibrium with the condensed phase; hence, a separate energy equation for the gas phase is not solved. It is noted that the gas phase continuity Eq. (4) is not directly solved. Instead, it is combined with the ideal gas equation of state and the Darcy equation to give a pressure evolution equation. When pressure is calculated form this equation, the gaseous mass flux is obtained using Darcy equation [44].

2.2. Evaporation models

The basics of the Arrhenius and equilibrium models are illustrated in the following two subsections.

2.2.1. Arrhenius model

In the Arrhenius model, liquid moisture is converted to water vapor through a first order chemical reaction-like process in which the rate is calculated by the Arrhenius equation:

$$\dot{\omega}_e''' = \rho_1 Z_1 \exp\left(\frac{-E_1}{RT}\right), \tag{6}$$

where ρ_1 is the density of liquid moisture. Here, $\dot{\omega}_e'''$ and $\dot{\omega}_1'''$ are used interchangeably, noting that the subscript $i = 1$ is for liquid moisture. Also, Z_1 and E_1 are pre-exponential factor and activation energy, respectively, in the heterogeneous reaction $k = 1$ corresponding to "evaporation reaction".

2.2.2. Equilibrium model

This model hypothesizes that the water vapor is in equilibrium with the liquid moisture at the local temperature. Moreover, at the saturation condition, the model assumes the water vapor partial pressure P_v is correlated with the water vapor saturation pressure P_{vs} by

$$P_v = a_w(T,U) P_{vs}, \tag{7}$$

where $a_w(T,U)$ is the water activity which is a function of temperature and fuel moisture content [51]. An analytical expression based on the Clausius-Clapeyron equation, $dP_{vs}/dT = P_{vs}\Delta h_{vap}/(RT^2)$ is used for the saturation pressure. Here, Δh_{vap} is the enthalpy of vaporization assumed to be a linear function of temperature, viz. $\Delta h_{vap} = A - BT$ [52]. Hence,

$$P_{vs}(T) = CT^{-\frac{B}{R}} \exp\left(\frac{-A}{RT}\right), \tag{8}$$

where $A = 5.72 \times 10^4$ kJ kmol^{-1}, $B = 45$ kJ kmol^{-1} K^{-1} and $C = 6.05 \times 10^{26}$ N m^{-2}, determined from steam tables [52]. Water activity is the ratio of water vapor pressure in the material to the pure water vapor pressure at a specific temperature. Its value ranges from zero to one with the upper limit corresponding to pure water. In other words, the water activity coefficient acts as a damping coefficient as it reduces the vapor pressure compared to the vapor saturation pressure when the FMC of the material falls below a value corresponding to the fiber saturation point. The following empirical correlation [18,30] was used for the water activity:

$$a_w(T,U) = \exp\Big\{\ 17.884 - 0.1423T + 23.63\times10^{-5}T^2 \times\left(1.0327 - 67.4\times10^{-5}T\right)^{92U}\Big\}, \tag{9}$$

for $U > 0$ and $T < 423.48$ K. This upper limit of temperature corresponds the upper limit of water activity, which is unit, in Eq. (9). To determine the evaporation rate, $\dot{\omega}_e''$ first, water vapor density is cal-

culated from the water vapor partial pressure through the ideal gas equation of state. Then, the mass conservation equation of the water vapor is applied. More details on this method are described in Section 2.4.

2.3. Computational methodology

The computational methodology utilized in this work is discussed here. Details on the equilibrium model computations are provided in Section 2.4. The discretized equations given in Gpyro [44] for shrinking one-dimensional objects are based on a finite volume method (FVM) formulation of Eqs. (1)–(5) with the cell size set to $\Delta z(t) = z_b(t) - z_t(t)$, the integrals approximated with a midpoint rule and the material time derivative approximated with an implicit Euler scheme. Fig. 1 shows a sample grid used by Gpyro with the cell center indicated by P. Cell P is surrounded by top and bottom cells, indicated by T and B, respectively. The subscripts t and b are used to denote the top and bottom faces of cell P, respectively.

With this notation, the discretized form of Eqs. (1)–(5) are:

$$\frac{(\bar{\rho}\Delta z)_P - (\bar{\rho}\Delta z)_P^0}{\Delta t} = -\left(\dot{\omega}_{fg}'''\Delta z\right)_P, \tag{10}$$

$$\frac{(\bar{\rho}Y_i\Delta z)_P - (\bar{\rho}Y_i\Delta z)_P^0}{\Delta t} = \left(\dot{\omega}_i'''\Delta z\right)_P, \tag{11}$$

$$\frac{(\bar{\rho}\bar{h}\Delta z)_P - (\bar{\rho}\bar{h}\Delta z)_P^0}{\Delta t} = -\dot{q}''|_b + \dot{q}''|_t - \left(\frac{\partial \dot{q}_r''}{\partial z}\Delta z\right)_P - \left(\dot{Q}_{s-g}'''\Delta z\right)_P + \sum_{k=1}^{K}\left(\dot{Q}_{s,k}'''\Delta z\right)_P + \sum_{i=1}^{M}\left(\dot{\omega}_i'''h_i\Delta z\right)_P, \tag{12}$$

$$\frac{\left(\rho_g\bar{\psi}\Delta z\right)_P - \left(\rho_g\bar{\psi}\Delta z\right)_P^0}{\Delta t} + \dot{m}''|_b - \dot{m}''|_t = \left(\dot{\omega}_{fg}'''\Delta z\right)_P, \tag{13}$$

$$\frac{\left(\rho_g\bar{\psi}Y_j\Delta z\right)_P - \left(\rho_g\bar{\psi}Y_j\Delta z\right)_P^0}{\Delta t} + \dot{m}''Y_j|_b - \dot{m}''Y_j|_t = -\dot{j}_j''|_b + \dot{j}_j''|_t + \left(\dot{\omega}_j'''\Delta z\right)_P, \tag{14}$$

where Δt is the time step, the superscript 0 indicates the variables in the previous time step, and $\dot{q}''$ and $\dot{q}_r''$ are conductive and in depth radiation heat fluxes, respectively, noting that $\dot{q}_t'' = \dot{q}_r'' + \dot{q}''$. Eqs. (10)–(14) are identical to those given in Ref. [44] for one dimensional objects experiencing shrinkage. An additional assumption which is used in Eqs. (13) and (14) but not stated in Ref. [44] is that V and $v_j \gg V_c$, i.e., the motion of the condensed phase is much slower than the gas phase. The velocity of the condensed phase is implicit in the Lagrangian derivative. Here, $\dot{m}'' = \rho_g\bar{\psi}V$ and $\rho_g Y_j\bar{\psi}v_j = \dot{m}''Y_j + \dot{j}_j''$, where $\dot{j}_j'' = -\rho_g\bar{\psi}D\partial Y_j/\partial z$ is the diffusive mass flux.

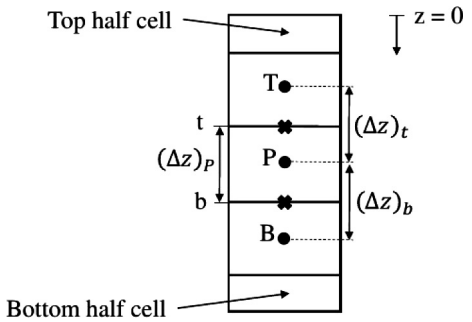

Fig. 1. Control volume system used for finite volume formulation.

2.4. Incorporation of the equilibrium model in Gpyro

An operator splitting technique, which was developed in this work to incorporate the equilibrium model in Gpyro, is illustrated here. Since the time integration scheme is implicit, the time discretization results in a system of nonlinear equations, which is solved iteratively in every time step. Each iteration consists of two stages, the reaction stage, which handles the evaporation and reaction terms, and the transport stage, which handles transport terms [31]. In the notation used, the variables calculated in the previous time step are denoted by superscript 0, the variables in the first stage are denoted by superscript $*$ and the variables in the second stage are indicated with no superscript.

In the reaction stage, the vapor saturation pressure P_{vs} and the vapor partial pressure P_v are calculated, using Eqs. (7)–(9). Then, water vapor density and mass fraction are calculated from $\rho_{v,P}^* = P_{v,P}M_v/RT_P$ and $Y_{v,P}^* = \rho_{v,P}^*/\rho_g$ where ρ_g is obtained from the ideal gas equation of state with the variables values available from the previous iteration. Here, the subscript v is used to indicate water vapor, which is equivalent to $j = 1$ as the index of the gaseous phase species. Then, the mass conservation equation of water vapor (see Eq. (14)) is used to calculate the evaporation rate of liquid water while excluding the transport terms:

$$\left(\dot{\omega}_e'''\Delta z\right)_P = \frac{(\rho_v\bar{\psi}\Delta z)_P^* - (\rho_v\bar{\psi}\Delta z)_P^0}{\Delta t}, \tag{15}$$

where $\bar{\psi}$ and Δz from the previous iteration are used to calculate $(\rho_v\bar{\psi}\Delta z)_P^*$. After calculating the evaporation rate, Eqs. (10) and (11) are used to update $(\bar{\rho}\Delta z)_P$ and $(\bar{\rho}Y_i\Delta z)_P$ for all condensed phase species. It should be noted that since the condensed phase mass and species conservation Eqs. (10) and (11) have no transport terms, their calculations are not split. Therefore, the starred value and the updated value of the variables computed from Eqs. (10) and (11) are the same, i.e. $(\bar{\rho}\Delta z)_P^* = (\bar{\rho}\Delta z)_P$ and $(\bar{\rho}Y_i\Delta z)_P^* = (\bar{\rho}Y_i\Delta z)_P$. Condensed phase species mass fractions, bulk density and cell size are updated, using $Y_{i,P} = (\bar{\rho}Y_i\Delta z)_P/(\bar{\rho}\Delta z)_P$, $\bar{\rho}_P = \left(\sum_i Y_{i,P}/\rho_{i,P}\right)^{-1}$ and $(\Delta z)_P = (\bar{\rho}\Delta z)_P/\bar{\rho}_P$, respectively, where $\rho_{i,P}$ is the bulk density of the condensed phase species i. To calculate the mass fractions of the rest of the gaseous species, i.e., $j = 2, \ldots, N$, in the reaction stage, the following equations are used:

$$\frac{\left(\rho_g\bar{\psi}\Delta z\right)_P^* - \left(\rho_g\bar{\psi}\Delta z\right)_P^0}{\Delta t} = \left(\dot{\omega}_{fg}'''\Delta z\right)_P, \tag{16}$$

$$\frac{\left(\rho_g\bar{\psi}Y_j\Delta z\right)_P^* - \left(\rho_g\bar{\psi}Y_j\Delta z\right)_P^0}{\Delta t} = \left(\dot{\omega}_j'''\Delta z\right)_P. \tag{17}$$

Specifically, Eq. (16) is multiplied by $Y_{j,P}^*$ and then subtracted from Eq. (17). Afterward, the resultant equation is solved for $Y_{j,P}^*$. The energy equation for the reaction stage is given as:

$$\frac{(\bar{\rho}\bar{h}\Delta z)_P^* - (\bar{\rho}\bar{h}\Delta z)_P^0}{\Delta t} = \left(\sum_{k=1}^{K}\dot{Q}_{s,k}'''\Delta z\right)_P + \sum_{i=1}^{M}\left(\dot{\omega}_i'''h_i\Delta z\right)_P. \tag{18}$$

From the equation above, $\bar{\rho}\bar{h}\Delta z\,{}_P^*$ is found and consequently the bulk enthalpy of the condensed phase associated with the evaporation and pyrolysis processes is calculated as: $\bar{h}_P^* = \bar{\rho}\bar{h}\Delta z\,{}_P^*/(\bar{\rho}\Delta z)_P$. The gaseous species mass fractions and the condensed phase bulk enthalpy calculated in the reaction stage are used in the solution of the equations in the transport stage.

In the transport stage, to solve for all the gaseous species mass fractions i.e., $j = 1, \ldots, N$, the gas phase continuity Eq. (19) is multiplied by $Y_{j,P}$ and then subtracted from the gas phase species conservation Eq. (20)

$$\frac{\left(\rho_g \bar{\psi} \Delta z\right)_P - \left(\rho_g \bar{\psi} \Delta z\right)_P^*}{\Delta t} + \dot{m}''|_b - \dot{m}''|_t = 0 \tag{19}$$

$$\frac{\left(\rho_g \bar{\psi} Y_j \Delta z\right)_P - \left(\rho_g \bar{\psi} Y_j \Delta z\right)_P^*}{\Delta t} + \dot{m}'' Y_j\big|_b - \dot{m}'' Y_j\big|_t = -\dot{j}''\Big|_b + \dot{j}''\Big|_t. \tag{20}$$

To solve for the temperature, the energy Eq. (21) is first solved for $\bar{h}$ after expressing the conductive heat fluxes in terms of enthalpy and then the temperature is extracted from the enthalpy

$$\frac{(\bar{\rho}\bar{h}\Delta z)_P - (\bar{\rho}\bar{h}\Delta z)_P^*}{\Delta t} = -\dot{q}''|_b + \dot{q}''|_t - \left(\dot{Q}'''_{s-g}\Delta z\right)_P - \left(\frac{\partial \dot{q}''_r}{\partial z}\Delta z\right)_P. \tag{21}$$

More details on the numerical methodology are given in [44].

3. Problem description

To validate the presented model, the experiment performed by Shen et al. [53] was set up in the modified Gpyro framework developed in the previous section. In the experiment, moist samples 100 mm × 100 mm × 15 mm in size were placed in a cone calorimeter apparatus and heated up by a radiant heater on one side while the other sides were insulated. Several thermocouples were placed at the surface and different points within the sample (1, 7 and 14 mm) to measure the temperature. Shen et al. [53] also simulated this experiment by a mathematical model (henceforth: Shen's model). They used the Arrhenius model for liquid moisture evaporation. Few, yet significant, differences exist between the present model and the Shen's model. First, the present model accounts for the transport of the gas phase by both convection and diffusion mechanisms while this is neglected in Shen's model. Moreover, unlike Shen's model, volume change is accounted for in the present model. Third, the energy Eq. (12) in the present model can take into account the effects of convective cooling due to the flow of volatiles and the in-depth radiation. These terms are lacking in Shen's model. The pyrolysis of wood to char and gases is described by a global two-stage reaction and is given in Table 1.

In this work, when the Arrhenius model was used for liquid moisture evaporation, the kinetic parameters were specified as $Z = 5.13 \times 10^{10}\ \mathrm{s}^{-1}, E = 88\ \mathrm{kJ\ mol}^{-1}$ and $\Delta h_e = -2260\ \mathrm{kJ\ kg}^{-1}$ for the corresponding reaction [10]. Shen's model used the same values for the pre-exponential factor and the activation energy but a slightly different value of $-2440\ \mathrm{kJ\ kg}^{-1}$ for the enthalpy of vaporization which was observed to have insignificant influence on the results of this study.

Fig. 2 shows a schematic of the computational setup. The condensed phase mass and species conservation equations do not need boundary conditions (BC) since they are treated in the Lagrangian framework and no spatial derivative terms appear in these equations. The top face BC for the condensed phase energy equation was achieved by establishing energy balance between contributing heat fluxes at the exposed surface:

$$-\bar{k}\frac{\partial T}{\partial z}\Big|_{z=0} = h_c(T_\infty - T|_{z=0}) + \bar{\epsilon}\sigma\left(T_\infty^4 - T^4\big|_{z=0}\right) + \alpha \dot{q}_e{}'', \tag{22}$$

where $\bar{k}$ is the bulk thermal conductivity, h_c is the top face convection heat transfer coefficient and equal to $10\ \mathrm{W\ m^{-2}\ K^{-1}}$, T_∞ is the ambient temperature, $\bar{\epsilon}$ is the bulk emissivity, α is the surface absorptivity, σ is the Stefan-Boltzman constant and $\dot{q}_e{}''$ is the incident radiant power supplied by an external source. The bottom face of the slab is insulated therefore zero heat flux condition was applied as the BC:

$$\frac{\partial T}{\partial z}\Big|_{z=\tau} = 0. \tag{23}$$

For the gaseous species mass conservation equation, the BC at the top face was obtained from the balance between diffusive and convective mass fluxes of the species:

$$-\bar{\psi}\rho_g D\frac{\partial Y_j}{\partial z}\Big|_{z=0} = h_m\left(Y_j^\infty - Y_j|_{z=0}\right), \tag{24}$$

where h_m is the mass transfer coefficient estimated as the ratio of the top face convection heat transfer coefficient to the gas phase specific heat capacity as h_c/c_{pg} and Y_j^∞ is the mass fraction of the jth species in the ambient. The bottom face of the slab was assumed to be impermeable and the corresponding BC was:

$$\frac{\partial Y_j}{\partial z}\Big|_{z=\tau} = 0. \tag{25}$$

Table 1
Reactions and kinetic parameters for pyrolysis of wood [53].

Reaction	Z (1/s)	E (kJ/mol)	Δh (kJ/kg)
wood → char	7.38×10^5	106.5	−420
wood → gases	1.44×10^4	88.6	−420

4. Results and discussion

Fig. 3 displays the temporal variation of the slab surface temperature for two sets of the results obtained in the current study with the equilibrium and Arrhenius models for liquid moisture evaporation. Additionally, Shen's modeling and experimental results [53] are included in this figure. The effect of the external radiant heat flux on the time evolution of the surface temperature is illustrated in Fig. 3(a)–(c) for heat fluxes of $30\ \mathrm{kW\ m^{-2}}, 40\ \mathrm{kW\ m^{-2}}$ and $60\ \mathrm{kW\ m^{-2}}$, respectively. The slab initial FMC was 15.3% in this case. For heat fluxes of $30\ \mathrm{kW\ m^{-2}}$ and $40\ \mathrm{kW\ m^{-2}}$, the match between the three models and the experiment was very good. For the highest heat flux level, all three models were still in a good agreement with the experiment, yet exhibiting some discrepancy. Fig. 3(d)–(f) depicts the impact of the slab initial FMC on the temporal variation of its surface temperature for FMC values of 5%, 15.3% and 26%, respectively when the external heat flux was $40\ \mathrm{kW\ m^{-2}}$. Evaporation is an endothermic

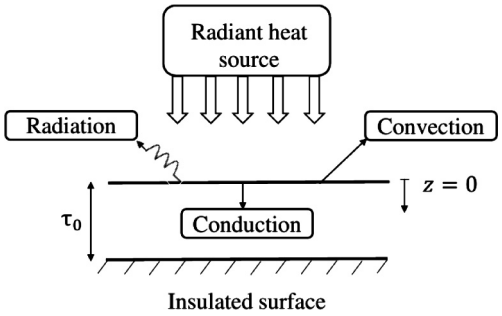

Fig. 2. A moist biomass slab with initial thickness of $\tau_0 = 15$ mm exposed to an external heat source on the top face while the bottom face is insulated.

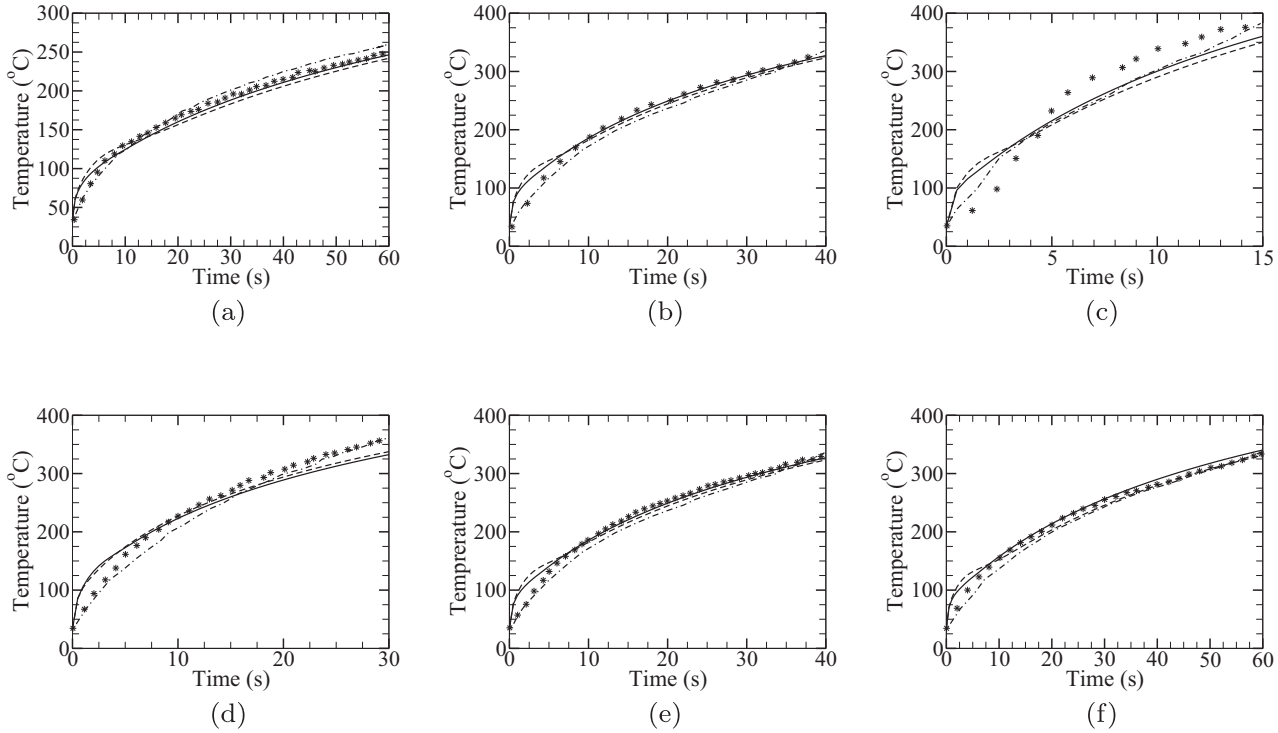

Fig. 3. Time evolution of the slab surface temperature for external radiant heat fluxes of (a) 30 kW m^{-2}, (b) 40 kW m^{-2} and (c) 60 kW m^{-2}, for initial FMC of 15.3%; and for initial FMC of (d) 5%, (e) 15.3% and (f) 26% for external radiant heat flux of 40 kW m^{-2}; experimental data (∗) and Arrhenius model (dashed-dotted line) of Shen et al. [53], and equilibrium model (solid line) and Arrhenius model (dashed line) of the present study.

process. Hence, it is expected that as the initial FMC increases, the surface temperature decreases because a larger fraction of the thermal energy supplied by the external source is consumed by evaporation rather than being used for sensible heating. This behavior was observed in all three modeling predictions as well as in the experiment. In Fig. 3(d), from the beginning to 5 s and from 15 s to the end, Shen's model produced a better prediction. From 5 s to 15 s the present model displayed a better match with the experiment. For the initial FMC of 15.3% and 26%, as seen in Fig. 3(e), (f), all models produced excellent predictions with respect to the experimental data. It can be seen in Fig. 3 that the surface temperatures for both equilibrium and Arrhenius models were virtually the same, which was attributed to the relatively low values of initial FMC in the simulations of this figure.

Fig. 4(a)–(c) shows the time evolution of the slab temperature for the same models and experiment at 1 mm, 7 mm and 14 mm below the surface, respectively, for an initial FMC of 15.3% and an external heat flux of 20 kW m^{-2}. Note the good agreement between the experimental data and the predictions of the equilibrium and Arrhenius models in the present study at $z = 1$ mm and $z = 7$ mm. At $z = 14$ mm, the Arrhenius model exhibited excellent agreement with the experimental data up to 300 s; it then deviated slightly. At this location, the equilibrium model was the only model that exhibited the same trend as the experiment throughout the simulation.

In fact, the radiation heat flux supplied by the heater in the experiments is non-uniform over the slab surface because it is observed that in the cone calorimeter experiments, initially ignition occurs only within a fraction of the slab exposed surface and then after several seconds flame spreads over the whole surface [54]. In the models, however, the external heat flux is assumed to be uniform over the sample exposed surface. Moreover, the discrepancy could be attributed to the uncertainty in the char density which was not provided in Ref. [53]. In the present work, char density reported in Ref. [49] was used. The char density affects thermal diffusivity of the fuel and in turn the temperature distribution.

Following the satisfactory validation study, Gpyro equipped with the operator splitting technique was used to provide a more detailed insight into the problem. An experiment in Ref. [53] for which the heat flux is 40 kW m^{-2} and the initial FMC is 26%, was chosen for further investigation. Another case with the same heat flux but with the initial FMC of 100% was also examined to extend the study to living fuels. Simulations were conducted using both equilibrium and Arrhenius models for liquid moisture evaporation. Therefore, a thorough quantitative comparison could be performed between the two evaporation models.

Fig. 5 shows spatial variations of evaporation rate, liquid moisture mass fraction and temperature at different times. In Fig. 5(a), (b), when the equilibrium model was used, the evaporation rate attained non-zero values only within a narrow region of the slab which was slightly widened as time elapsed. In contrast, evaporation rate profiles obtained by the Arrhenius model were broad and smooth which was a result of the exponential term in the mathematical expression of the corresponding rate Eq. (6). Although this smooth behavior is advantageous regarding numerical stability of the simulation, it doesn't have sound physical basis. Both models exhibited the same trend of decrease in the maximum rate as the distance from the exposed surface increased. This is because at the slab surface and the points close to it, the external heat transfer was dominant whereas at the points deeper within the slab, the internal heat transfer was dominant. Rates were larger for higher initial FMC because more liquid moisture was available to be vaporized. This behavior was more pronounced for the equilibrium model. On the other hand, evaporation front proceeded faster in the slab with lower initial FMC. At a fixed initial FMC, front velocity was virtually the same for both evaporation models. The liquid moisture mass fraction profiles are depicted in Fig. 5(c), (d). It is seen that, unlike the Arrhenius model, the equilibrium model

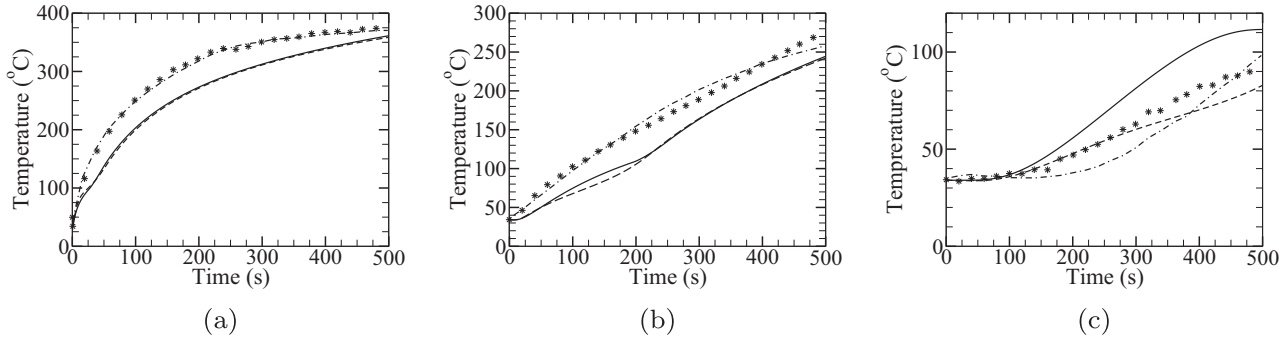

Fig. 4. Time evolution of temperature at (a) $z = 1$ mm, (b) $z = 7$ mm and (c) $z = 14$ mm for initial FMC of 15.3% and external radiant heat flux of 20 kW m^{-2}; experimental data (∗) and Arrhenius model (dashed-dotted line) of Shen et al. [53], and equilibrium model (solid line) and Arrhenius model (dashed line) of the present study.

exhibited a steep evaporation front. For example, in Fig. 5(c) at $t = 250$ s, the evaporation zone extended from $z = 6.2$ mm to $z = 7.1$ mm (or a 0.9 mm thick zone) for the equilibrium model while the zone extended from $z = 5.8$ mm to the bottom face of the slab (implying a 7.4 mm thick zone) for the Arrhenius model. With the equilibrium model, evaporation took place within a thin region that could be approximated as a slice, compared to a thick region where evaporation took place in the Arrehnius model. Fig. 5(e), (f) displays the temperature profiles. When the equilibrium model was used, an abrupt change in the slope of the temperature profiles was observed. This was due to the endothermicity of the evaporation process and was associated with the location of the evaporation front. Between the exposed surface and the evaporation front, temperature gradients were more pronounced, indicating internal heat transfer was the dominant mechanism. In the wet zone where the liquid moisture mass fraction was equal to its initial value, temperature gradients were very small because of high thermal capacity of water. When the Arrhenius model was used, evaporation commenced at temperatures below the normal boiling point; e.g. it started from about 50 °C at $t = 50$ s for both cases. This is another drawback of the Arrhenius model for high heating rate problems [19]. At a specific time, the Arrhenius model predicted lower temperature. This observation was more noticeable for the higher initial FMC, specifically through the region with small temperature gradients. According to Fig. 5(c), (d), in this region, the equilibrium model displayed no evaporation whereas the Arrhenius model showed evaporation. As an endothermic process, evaporation lowered the temperature as seen in Fig. 5(e), (f).

Time histories of evaporation rate, liquid moisture mass fraction and temperature at different locations are presented in Fig. 6. It is seen in Fig. 6(a), (b) that the rate peak values for the equilibrium model were appreciably larger. Furthermore, the rate peak value increased as distance to the heated surface decreased. The impetus for evaporation was the heating source and locations closer to the surface realized the effect of the source more significantly. Note that in Fig. 6(b) at $z = 14$ mm, for the equilibrium model, the rate value was zero at all times while for the Arrhenius model, it had non-zero, yet very small values. The rate time histories from the equilibrium model illustrated that evaporation started later at a specific location for the higher initial FMC due to higher fuel heat capacity. Consequently, it took more time for a location to reach a temperature at which evaporation commenced. This physical behavior, however, was not observed in the rate time histories predicted by the Arrhenius model. Fig. 6 (c), (d) shows that when the equilibrium model is implemented, at a specific location, the biomass slab lost its moisture more rapidly because of higher vaporization rates. Moreover, it can be seen that at a given location, the drying time increased with the initial FMC since the liquid moisture mass was larger for larger initial FMC. It was observed in Fig. 6(e), (f) that as the distance from the exposed surface increased, the thermal resistance increased and consequently, the temperature decreased. Moreover, it is seen that the temperatures predicted by the Arrhenius model were slightly lower and the difference between the solid and the dashed lines became more apparent with increasing depth from the exposed surface. The reason is that when the Arrhenius model was used, the evaporation process at a specific location took a significantly longer time which increased as the distance from the fuel surface increased, as could be seen in Fig. 6(a), (b). Also, since evaporation is an endothermic process, the endothermicity effect of the evaporation prevailed longer, which resulted in lower temperatures. This effect is more visible for higher initial FMC as shown in Fig. 6(f). Note in this figure that for the Arrhenius model and at $z = 14$ mm, the slab temperature was quite below the water normal boiling point at all times, yet evaporation took place which was inconsistent with the physics of evaporation.

Fig. 7 displays dry fuel and char mass fraction profiles at three different times. After exposure to the external heat source, the slab surface temperature rose and heat was transferred inward by conduction and radiation. Meanwhile, the liquid moisture began to vaporize at the surface, leading to the formation of an evaporation front that moves inward. When the surface temperature was sufficiently high, biomass degradation commenced and a pyrolysis zone was formed. As the pyrolysis zone moved inward, a char layer was formed and this layer thickened. As observed in Fig. 7(a), in the equilibrium model, five zones existed simultaneously within the particle: (i) the char layer where dry fuel mass fraction was zero, (ii) the pyrolyzing zone where dry fuel mass fraction varied from zero to one, (iii) the dry zone where dry fuel mass fraction was one, (iv) the drying zone where dry fuel mass fraction decreased from one to its initial value, and (v) the wet zone where dry fuel and liquid moisture mass fractions were equal to their initial values. In Fig. 7(b), the char layer has not been formed yet because of the higher initial FMC resulting in lower temperature and in turn lower reaction rate. In the Arrhenius model, the drying zone was significantly widened and no wet zone was observed, as shown in Fig. 7(a). The equilibrium model results were more consistent with those of previous works [55,8,29]. In Fig. 7(c), (d) at a specific time, the equilibrium model predicted a slightly higher char yield because of a higher predicted temperature, as seen in Fig. 5(e), (f), resulting in a larger reaction rate. Nonetheless, char distribution within the slab was found insensitive to the evaporation model compared to dry fuel distribution.

The mass loss rate (MLR) of the fuel slab is shown in Fig. 8. The MLR exhibited two peaks: the first was attributed to the liquid moisture evaporation and the second to the dry fuel pyrolysis. For the cases with higher initial FMC, the first peak attained a higher value since evaporation occured with higher rates, as shown

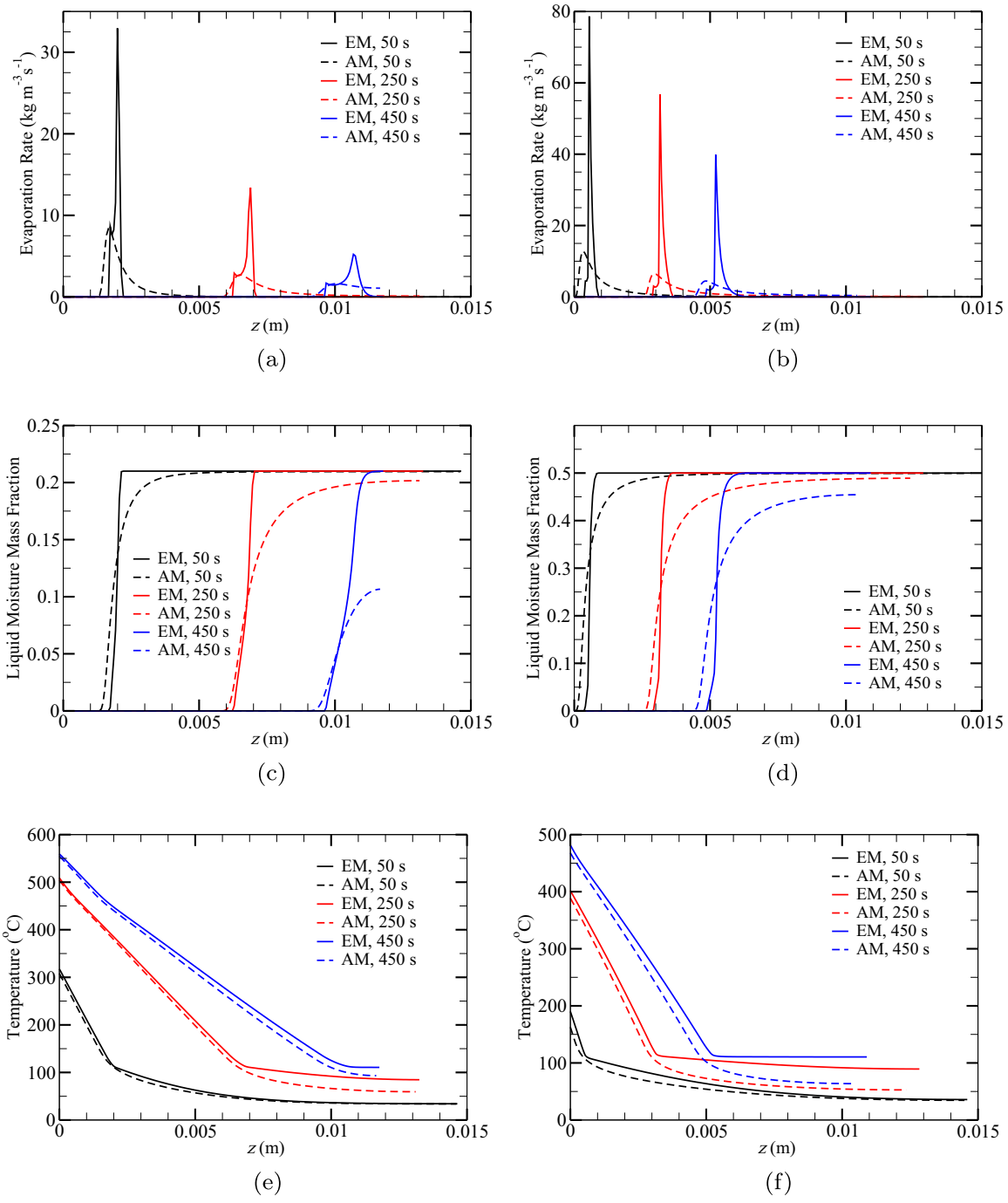

Fig. 5. Profiles of (a,b) evaporation rate (c,d) liquid moisture mass fraction and (e,f) temperature for external radiant heat flux of 40 kW m^{-2}, initial FMC of 26% (left column) and initial FMC of 100% (right column); EM: Equilibrium Model, AM: Arrhenius Model.

in Fig. 5(a) and (b). For these cases, the second peak had lower values because it was mainly influenced by pyrolysis with a rate depending on the slab temperature, which was lower for the cases with higher initial FMC. Additionally, the peaks occurred at later times when the initial FMC increased. It can be argued that it took longer for the slab to reach the temperatures at which evaporation and pyrolysis started. For a given initial FMC, the first peak was higher for the Arrhenius model since the fuel initially lost more moisture in this model, as seen in Fig. 5(c), (d). In contrast, the equilibrium model for 100% FMC showed a higher value for the second peak because this model resulted in higher temperatures and in turn greater pyrolysis rates, as could be seen in Fig. 5(e), (f).

Fig. 9(a) shows the slab's total shrinkage against the external heat flux, where it is calculated as $\tau_0 - \tau_f / \tau_0 \times 100\%$ where τ_0 is the slab initial thickness and τ_f is the slab final thickness. Overall, the total shrinkage increased with the heat flux level because at a higher heat flux, more liquid moisture was vaporized and more dry fuel was degraded and converted to char and pyrolysis gases. For a specific heat flux, the Arrhenius model showed a slightly higher shrinkage since when this model was used, overall the slab lost more moisture (see Fig. 5(c), (d)). The effect of initial FMC on the slab total shrinkage is depicted in Fig. 9(b). It is observed that the total shrinkage increased with the initial FMC. It can be argued that the slab with higher initial FMC has more liquid mass which is

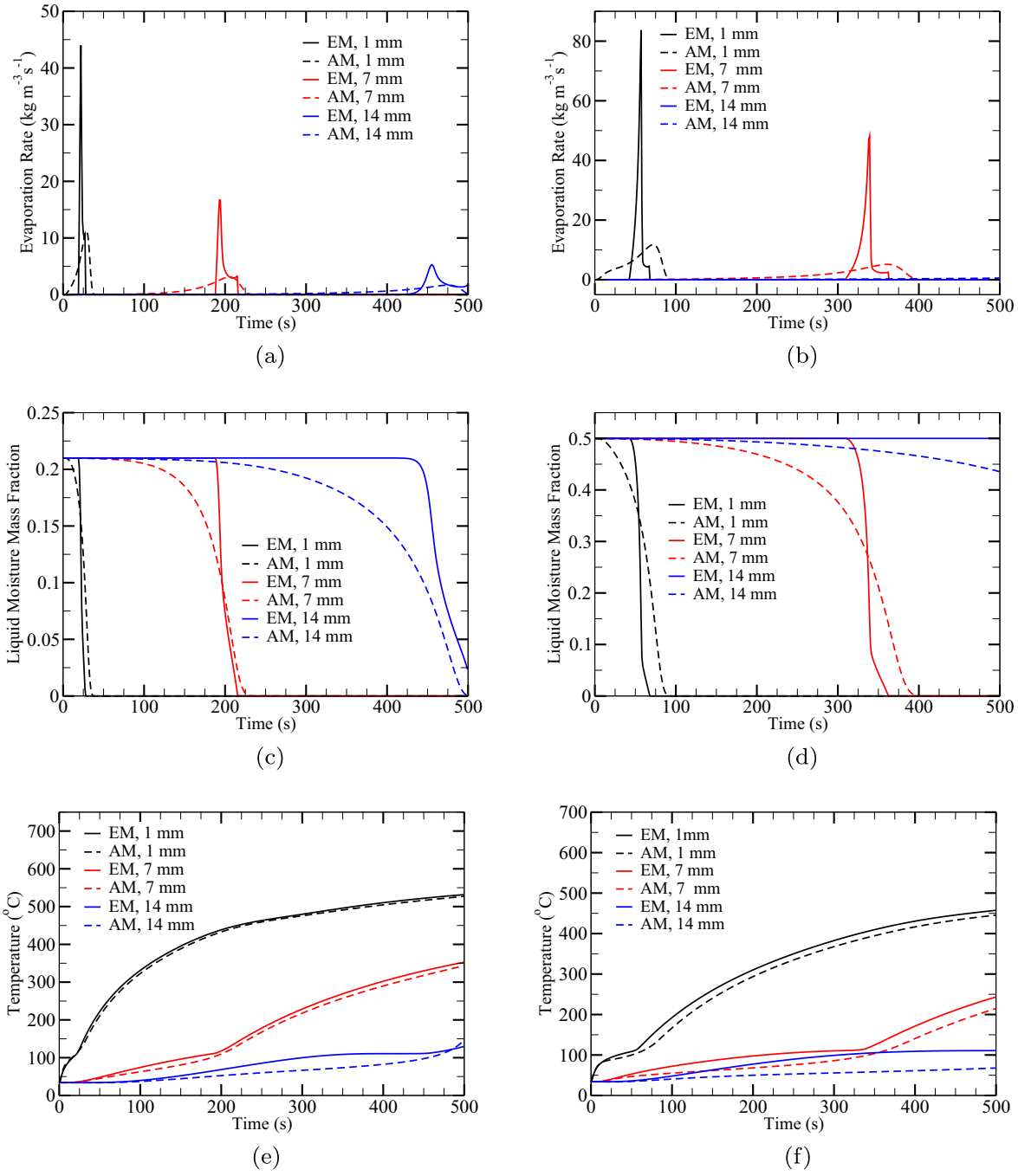

Fig. 6. Time histories of (a,b) evaporation rate (c,d) liquid moisture mass fraction and (e,f) temperature for external radiant heat flux of 40 kW m^{-2}, initial FMC of 26% (left column) and initial FMC of 100% (right column); EM: Equilibrium Model, AM: Arrhenius Model.

released as the water vapor and thus causes more shrinkage. For initial FMC below 30%, both evaporation models predicted a nearly equal amount of total shrinkage whereas for initial FMC above 30%, the difference in the predicted shrinkage between the models was appreciable and increased with initial FMC.

The slab total shrinkage is a consequence of change in the size of computational cells. According to the condensed phase conservation of mass (Eq. 10), when a cell experiences any mass loss by means of evaporation, pyrolysis or both, its size changes. In this work, size change occurred only in the form of shrinkage. The relative change in the cell size was called the local shrinkage and calculated as $(\Delta z_0 - \Delta z)/\Delta z_0 \times 100\%$ where Δz_0 and Δz were the initial size and the instantaneous size of the cell, respectively. Local shrinkage is plotted throughout the slab at different times in Fig. 10. At an early time; e.g. $t = 50$ s, the slab temperature was not high enough for pyrolysis to occur. Thus, shrinkage was caused only by liquid moisture loss. At this time, cells that were completely dried experienced a ~15% reduction in their size while cells in the wet zone experienced no shrinkage. At later times, wood decomposition and char formation occured within a portion of the slab, resulting in further shrinkage in the corresponding cells (locations). The cells on, and close to, the surface attained the most shrinkage, which was about 40%. Generally, the more char formed in a cell, the more shrinkage occurred. The evaporation models did not exhibit a significant difference in the local shrinkage where evaporation had completed. Both models showed that when a cell

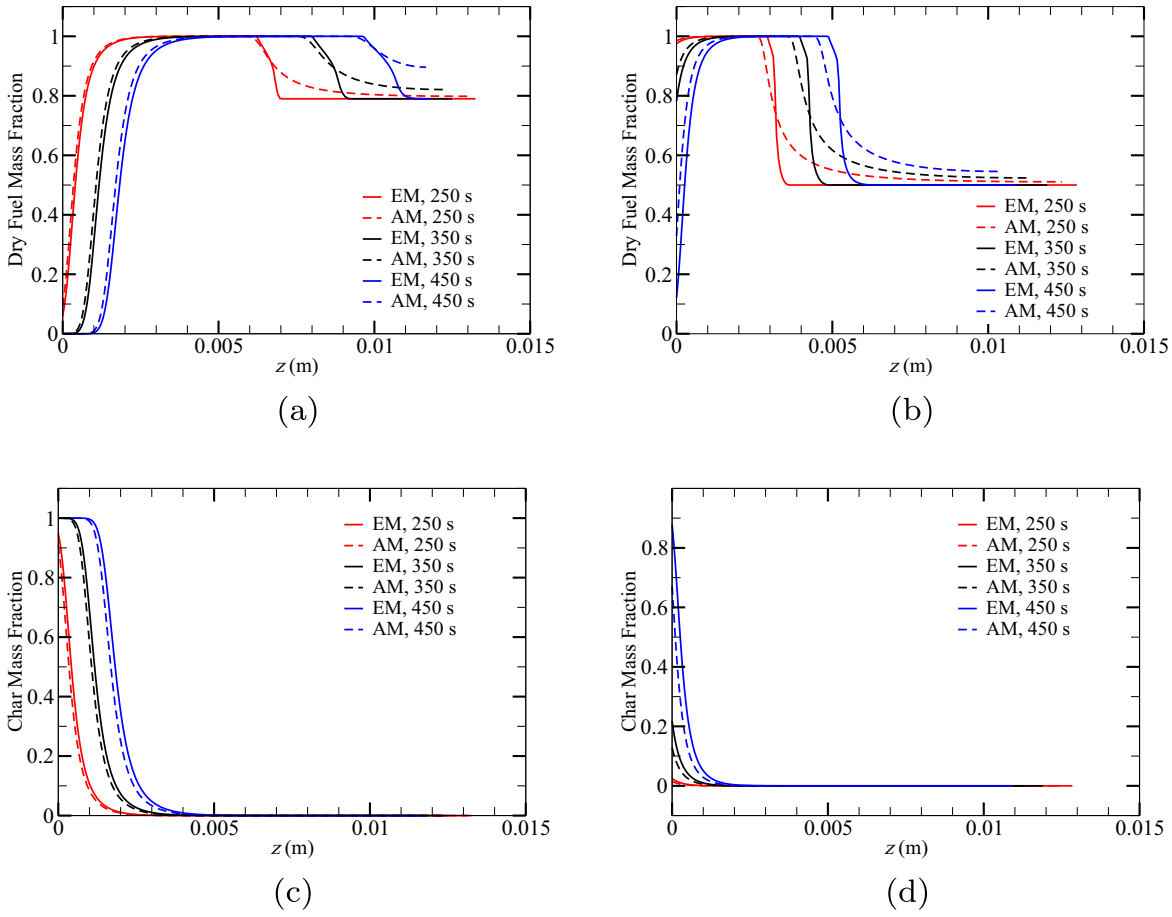

Fig. 7. Profiles of (a) dry fuel mass fraction in FMC of 26%; (b) dry fuel mass fraction in FMC of 100%; (c) char mass fraction in FMC of 26%; and (d) char mass fraction in FMC of 100% for external radiant heat flux of 40 kW m^{-2}; EM: Equilibrium Model, AM: Arrhenius Model.

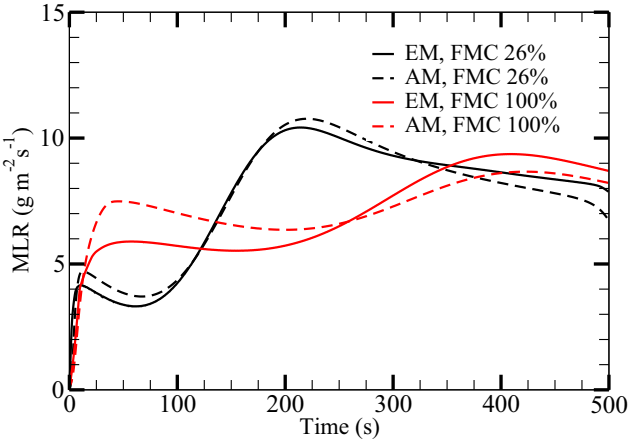

Fig. 8. Mass loss rate of the fuel slab for external radiant heat flux of 40 kW m^{-2}; EM: Equilibrium Model, AM: Arrhenius Model.

lost its liquid moisture, its size shrank to 85% of its initial size. However, because the Arrhenius model resulted in a broader evaporation zone, more locations experienced shrinkage. For example, at $t = 250$ s, when the Arrhenius model was used, every single location throughout the slab underwent shrinkage whereas when the equilibrium model was used, a region in the slab that spanned from $z = 7$ mm to the bottom face (the wet zone) observed no shrinkage.

In the apparatus used to conduct the experiment, the fuel slab was situated on a fixed sample holder. Therefore, as it was heated and underwent shrinkage, its top face moved downward and receded whereas its bottom face remained stationary. In the simulation, however, the top face was assumed fixed as the origin of the coordinate system. Thus, the bottom face moved toward the top face as the slab evolved thermochemically. Nonetheless, the shrinkage rate defined as the rate at which the top and bottom faces approached each other was independent of the choice of the coordinate system. As shown in Fig. 10, at a specific time during the simulation, a fraction of computational cells shrank in size and as a result, the distance between the top and bottom surfaces reduced. The surface recession rate, is shown as a function of time in Fig. 11. At the beginning, the recession rate increased rapidly and attained a local maxima which was due to evaporation. This peak value occurred at a later time for higher FMC since in this case, evaporation progressed more slowly. After a few minutes, the recession rate exhibited the second local maxima which was attributed to dry fuel pyrolysis. The fuel slab with higher FMC attained a higher surface recession rate since during simulation, it shrank more, as seen in Fig. 9(b). Furthermore, as long as evaporation significantly contributed to the overall mass loss, the sensitivity of surface recession rate to the evaporation model was noticeable for higher FMC.

5. Summary and conclusions

The thermochemical evolution of a moist shrinking biomass slab subject to radiant heating was investigated after extending

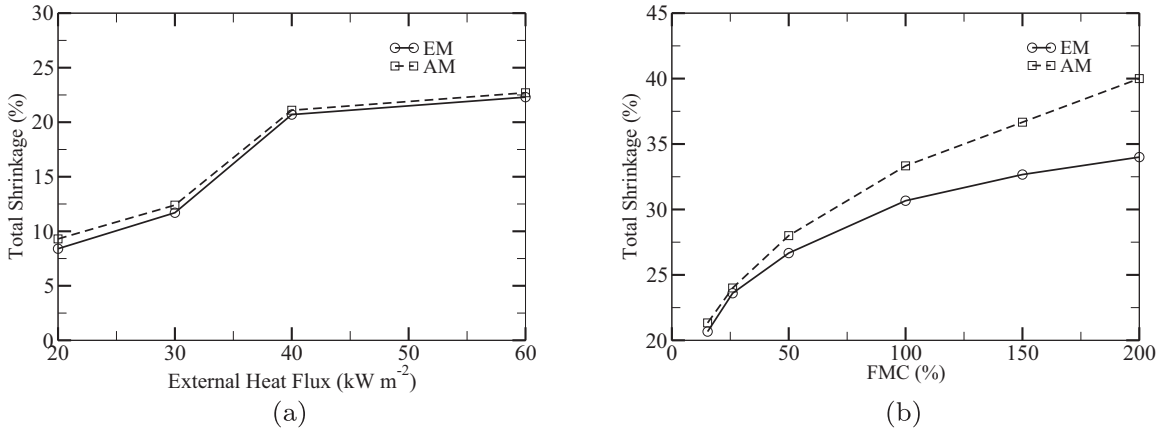

Fig. 9. The total shrinkage versus (a) external heat flux for fixed initial FMC of 15.3%; and (b) FMC for fixd external heat flux of 40 kW/m^2; EM: Equilibrium Model, AM: Arrhenius Model.

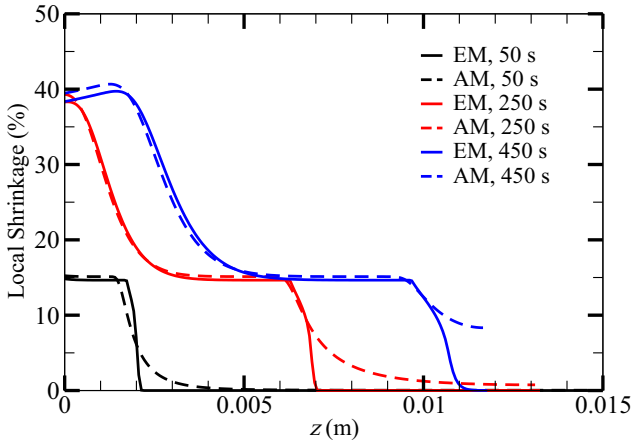

Fig. 10. Local shrinkage for external heat flux of 40 kW m^{-2} and initial FMC of 26%; EM: Equilibrium Model, AM: Arrhenius Model.

an existing pyrolysis computational framework, Gpyro to include the equilibrium model for liquid moisture evaporation. In the present study, also, a continuum description of mass and energy conservation for a pyrolyzating, shrinking porous medium was provided in the form of integral-differential equations. The model

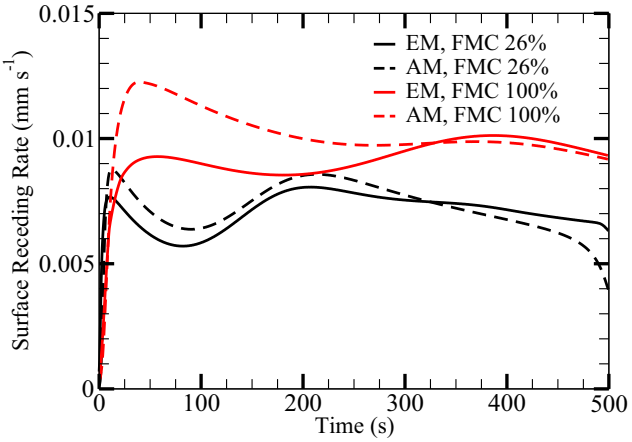

Fig. 11. Time history of the fuel surface recession rate for external heat flux of 40 kW m^{-2} and initial FMC of 26% and 100%; EM: Equilibrium Model, AM: Arrhenius model.

was favorably validated against cone calorimeter experiments conducted by Shen et al. [53] by comparing the simulation results with the experimental data for temperatures at different locations of the fuel slab. Drying dynamics in the fuel slab with moisture content as simulated by the equilibrium model and the widely used Arrhenius model were studied. The equilibrium model took into account the saturated condition at which evaporation occured whereas the Arrhenius model simply assumed that evaporation occured through a chemical reaction. The study examined two initial FMCs of 26% and 100% representing dead and live fuels, respectively. The propagation of a steep evaporation front where evaporation rate, liquid moisture mass fraction and temperature profiles exhibited large spatial gradients characterized the equilibrium model. The Arrhenius model, however, exhibited a smooth behavior throughout the fuel particle as a result of the mathematical expression of the evaporation rate. The comparative study of the evaporation modeling approaches illustrated that the equilibrium model much better represented the underlying physics of evaporation. The equilibrium model demonstrated evaporation as a surface phenomenon, did not exhibit evaporation below the normal boiling point of water and properly showed the impact of the change in the initial FMC on the drying dynamics. Furthermore, in the equilibrium model, a distinguishable wet zone characterized by moisture content equivalent to the initial FMC, was observed in the slab. The presence of such zone during the thermochemical conversion of biomass has been reported in the previous works [55,8,29]. The Arrhenius model was not able to capture this zone. The choice of evaporation model had an insignificant impact on the amount of shrinkage in the low-FMC fuel and an appreciable impact in the high-FMC fuel. The simulation results also demonstrated that regardless of the evaporation model, the fuel shrinkage increased when the external heat flux or the initial FMC increased.

Declaration of Competing Interest

None.

Acknowledgements

This work was supported by DOD/EPA/DOE Strategic Environmental Research and Development Program Project RC-2640 administered by the USDA Forest Service PSW Research Station through cooperative agreement 16-JV-11272167-025 with The University of Alabama in Huntsville.

Appendix A. Supplementary material

Supplementary data associated with this article can be found, in the online version, at https://doi.org/10.1016/j.ijheatmasstransfer.2019.118672.

References

[1] A.C. Scott, D.M.J.S. Bowman, W.J. Bond, S.J. Pyne, M.E. Alexander, Fire on Earth: An Introduction, John Wiley & Sons, Inc, 2014.
[2] E.A. Johnson, K. Miyanishi (Eds.), Forest Fires: Behavior and Ecological Effects, Academic Press, London, UK, 2001, 79-149. https://doi.org/10.1016/B978-012386660-8/50006-4.
[3] D.R. Weise, C.S. Wright, Wildland fire emissions, carbon and climate: characterizing wildland fuels, For. Ecol. Manage. 317 (2014) 26–40.
[4] R. Miller, J. Bellan, A generalized biomass pyrolysis model based on superimposed cellulose, hemicelluloseand liqnin kinetics, Combust. Sci. Technol. 126 (1997) 97–137.
[5] Y. Qi, W.M. Jolly, P.E. Dennison, R.C. Kropp, Seasonal relationships between foliar moisture content, heat content and biochemistry of lodgepole line and big sagebrush foliage, Int. J. Wildland Fire 25 (2016) 574–578.
[6] B. Yashwanth, B. Shotorban, S. Mahalingam, C. Lautenberger, D. Weise, A numerical investigation of the influence of radiation and moisture content on pyrolysis and ignition of a leaf-like fuel element, Combust. Flame 163 (2016) 301–316.
[7] R.B. Bates, A.F. Ghoniem, Modeling kinetics-transport interactions during biomass torrefaction: the effects of temperature, particle size, and moisture content, Fuel 137 (2014) 216–229.
[8] K.M. Bryden, M.J. Hagge, Modeling the combined impact of moisture and char shrinkage on the pyrolysis of a biomass particle, Fuel 82 (2003) 1633–1644.
[9] S.C. Ferguson, A. Dahale, B. Shotorban, S. Mahalingam, D.R. Weise, The role of moisture on combustion of pyrolysis gases in wildland fires, Combust. Sci. Technol. 185 (2013) 435–453.
[10] B. Shotorban, B.L. Yashwanth, S. Mahalingam, D.J. Haring, An investigation of pyrolysis and ignition of moist leaf-like fuel subject to convective heating, Combust. Flame 190 (2018) 25–35.
[11] W.-C.R. Chan, M. Kelbon, B.B. Krieger, Modelling and experimental verification of physical and chemical processes during pyrolysis of a large biomass particle, Fuel 64 (1985) 1505–1513.
[12] H. Lu, W. Robert, G. Peirce, B. Ripa, L.L. Baxter, Comprehensive study of biomass particle combustion, Energy Fuels 22 (2008) 2826–2839.
[13] C. Lautenberger, C. Fernandez-Pello, Generalized pyrolysis model for combustible solids, Fire Saf. J. 44 (2009) 819–839.
[14] C. Anand, B. Shotorban, S. Mahalingam, S. McAllister, D. Weise, Physics-based modeling of live wildland fuel ignition experiments in the forced ignition and flame spread test apparatus, Combust. Sci. Technol. 189 (2017) 1551–1570.
[15] X.D. Chen, A. Putranto, Reaction engineering approach (rea) to modeling drying problems: Recent development and implementations, Drying Technol. 33 (2015) 1899–1910.
[16] K.M. Bryden, K.W. Ragland, C.J. Rutland, Modeling thermally thick pyrolysis of wood, Biomass Bioenergy 22 (2002) 41–53.
[17] M.J. Prins, K.J. Ptasinski, F.J. Janssen, Torrefaction of wood: Part 1. Weight loss kinetics, J. Anal. Appl. Pyrol. 77 (2006) 28–34.
[18] C. Di Blasi, Simultaneous heat, mass and momentum transfer during biomass drying, in: Developments in Thermochemical Biomass Conversion, Springer, 1997, pp. 117–131.
[19] B. Peters, C. Bruch, A flexible and stable numerical method for simulating the thermal decomposition of wood particles, Chemosphere 42 (2001) 481–490.
[20] A. Putranto, X.D. Chen, S-REA (spatial reaction engineering approach): An effective approach to model drying, baking and water vapor sorption processes, Chem. Eng. Res. Des. 101 (2015) 135–145.
[21] A. Kharaghani, K.H. Le, T.T.H. Tran, E. Tsotsas, Reaction engineering approach for modeling single wood particle drying at elevated air temperature, Chem. Eng. Sci. 199 (2019) 602–612.
[22] P.K. Agarwal, W.E. Genetti, Y.Y. Lee, Coupled drying and devolatilization of wet coal in fluidized beds, Chem. Eng. Sci. 41 (1986) 2373–2383.
[23] J. Saastamoinen, J.-R. Richard, Simultaneous drying and pyrolysis of solid fuel particles, Combust. Flame 106 (1996) 288–300.
[24] B. Peters, E. Schröder, C. Bruch, T. Nussbaumer, Measurements and particle resolved modelling of heat-up and drying of a packed bed, Biomass Bioenergy 23 (2002) 291–306.
[25] A.H. Mahmoudi, F. Hoffmann, B. Peters, Detailed numerical modeling of pyrolysis in a heterogeneous packed bed using xdem, J. Anal. Appl. Pyrol. 106 (2014) 9–20.
[26] M.R. Karim, A.A. Bhuiyan, J. Naser, Effect of recycled flue gas ratios for pellet type biomass combustion in a packed bed furnace, Int. J. Heat Mass Transf. 120 (2018) 1031–1043.
[27] M. Bellais, Modelling of the Pyrolysis of Large Wood Particles (Ph.D. thesis), KTH, 2007.
[28] J. Saastamoinen, J. Richard, Drying, pyrolysis and combustion of biomass particles, in: Research in Thermochemical Biomass Conversion, Springer, 1988, pp. 221–235.
[29] A. Galgano, C. Di Blasi, Modeling the propagation of drying and decomposition fronts in wood, Combust. Flame 139 (2004) 16–27.
[30] S.B. Nasrallah, P. Perre, Detailed study of a model of heat and mass transfer during convective drying of porous media, Int. J. Heat Mass Transf. 31 (1988) 957–967.
[31] C. Di Blasi, Multi-phase moisture transfer in the high-temperature drying of wood particles, Chem. Eng. Sci. 53 (1998) 353–366.
[32] B. Moghtaderi, B.Z. Dlugogorski, E.M. Kennedy, D. Fletcher, Effects of the structural properties of solid fuels on their re-ignition characteristics, Fire Mater. 22 (1998) 155–165.
[33] M.G. Grønli, M.C. Melaaen, Mathematical model for wood pyrolysis comparison of experimental measurements with model predictions, Energy Fuels 14 (2000) 791–800.
[34] J.C. Wurzenberger, S. Wallner, H. Raupenstrauch, J.G. Khinast, Thermal conversion of biomass: comprehensive reactor and particle modeling, AIChE J. 48 (2002) 2398–2411.
[35] N. Zobel, The Representative Particle Model (Ph.D. Thesis), Technische Universität Berlin, 2007.
[36] K.H. Le, E. Tsotsas, A. Kharaghani, Continuum-scale modeling of superheated steam drying of cellular plant porous media, Int. J. Heat Mass Transf. 124 (2018) 1033–1044.
[37] W. Massman, Modeling soil heating and moisture transport under extreme conditions: Forest fires and slash pile burns, Water Resour. Res. 48 (2012).
[38] W. Massman, A non-equilibrium model for soil heating and moisture transport during extreme surface heating: the soil (heat-moisture-vapor) HMV-model version, Geoscientific Model Development. 8 (2015) 3659–3680.
[39] M. Melaaen, Numerical analysis of heat and mass transfer in drying and pyrolysis of porous media, Numer. Heat Transf. Part A Appl. 29 (1996) 331–355.
[40] L.R. Petzold, A differential/algebraic system solver, 1991.
[41] K.H. Karlsen, K.-A. Lie, J.R. Natvig, H.F. Nordhaug, H.K. Dahle, Operator splitting methods for systems of convection-diffusion equations: nonlinear error mechanisms and correction strategies, J. Comput. Phys. 173 (2001) 636–663.
[42] D. Lanser, J.G. Verwer, Analysis of operator splitting for advection–diffusion–reaction problems from air pollution modelling, J. Comput. Appl. Math. 111 (1999) 201–216.
[43] B. Sportisse, An analysis of operator splitting techniques in the stiff case, J. Comput. Phys. 161 (2000) 140–168.
[44] C. Lautenberger, Gpyro–A Generalized Pyrolysis Model for Combustible Solids, Technical Reference Version 0.8, Reax Engineering Inc., Berkeley, CA, 2014.
[45] X. Huang, G. Rein, H. Chen, Computational smoldering combustion: predicting the roles of moisture and inert contents in peat wildfires, Proc. Combust. Inst. 35 (2015) 2673–2681.
[46] X. Huang, G. Rein, Thermochemical conversion of biomass in smouldering combustion across scales: The roles of heterogeneous kinetics, oxygen and transport phenomena, Bioresour. Technol. 207 (2016) 409–421.
[47] T.C. Mulky, K.E. Niemeyer, Computational study of the effects of density, fuel content, and moisture content on smoldering propagation of cellulose and hemicellulose mixtures, Proc. Combust. Inst. 37 (2019) 4091–4098.
[48] Y. Ding, R. Zhou, C. Wang, K. Lu, S. Lu, Modeling and analysis of bench-scale pyrolysis of lignocellulosic biomass based on merge thickness, Bioresour. Technol. 268 (2018) 77–80.
[49] C. Lautenberger, C. Fernandez-Pello, A model for the oxidative pyrolysis of wood, Combust. Flame 156 (2009) 1503–1513.
[50] P. Perre, I. Turner, R. Rémond, Comprehensive drying models based on volume-averaging: background, application and perspective, Modern Drying Technology 1 (2007) 1–55.
[51] A.-L. Lozano, F. Cherblanc, B. Cousin, J.-C. Bénet, Experimental study and modelling of the water phase change kinetics in soils, Eur. J. Soil Sci. 59 (2008) 939–949.
[52] M.S. Sahota, Heat and Mass Transfer in Porous Concrete Structure Subject to Fire (Ph.D. Thesis), University of California, Berkeley, Department of Mechanical Engineering, 1976.
[53] D. Shen, M. Fang, Z. Luo, K. Cen, Modeling pyrolysis of wet wood under external heat flux, Fire Saf. J. 42 (2007) 210–217.
[54] S.I. Stoliarov, S. Crowley, R.E. Lyon, G.T. Linteris, Prediction of the burning rates of non-charring polymers, Combust. Flame 156 (2009) 1068–1083.
[55] R. Bilbao, J. Mastral, J. Ceamanos, M. Aldea, Modelling of the pyrolysis of wet wood, J. Anal. Appl. Pyrol. 36 (1996) 81–97.